Small Structures

small structures

www.small-structures.com

RESEARCH ARTICLE OPEN ACCESS

A Knittable Neural-Inspired MXene-Aramid Fiber for Wearable High-Fidelity Signal Transmission

Jizhen Zhang[1,2,3] | Sitarama Kada[2] | Jian Tang[4] | Jinlong Tao[1] | Peter A. Lynch[2] | Renzhi Ma[3] | Joselito M. Razal[2,5]

[1]Hainan Provincial Key Laboratory of Natural Rubber Processing, Agricultural Products Processing Research Institute, Chinese Academy of Tropical Agricultural Sciences, Zhanjiang, P. R. China | [2]Australian Synchrotrons, ANSTO, Clayton, Australia | [3]Research Center for Materials Nanoarchitectonics, National Institute for Materials Science, Tsukuba, Japan | [4]Institute of Advanced Machines, Zhejiang University, Hangzhou, China | [5]Joint Research Centre for Fiber Innovations and Renewable Materials, School of Fashion and Textiles, The Hong Kong Polytechnic University, Hong Kong SAR, China

Correspondence: Peter A. Lynch (peter.lynch@deakin.edu.au) | Joselito M. Razal (joselito.razal@polyu.edu.hk)

Received: 15 December 2025 | **Revised:** 4 February 2026 | **Accepted:** 6 February 2026

Keywords: aramid nanofiber | coaxial fiber | knittable | MXene | signal transfer | smart textile

ABSTRACT

Knittable conductive fibers have emerged as key components for multifunctional textiles used in energy storage, sensing, and protective wear. A persistent challenge in this field, however, is maintaining signal integrity across extended distances within smart textiles. To address this limitation, a core–sheath fiber consisting of a conductive MXene core encapsulated within a mechanically robust aramid nanofiber (ANF) sheath is strategically designed, with each component serving a distinct functional role. We systematically investigate the coagulation process responsible for forming this hierarchical structure and characterize its effect on fiber morphology. The ANF sheath enhances thermal and environmental stability while serving as a protective barrier for the MXene core. This design enables consistent electrical conductivity even after 250 days of air exposure and over 5000 bending cycles. Micro-computed tomography analysis confirms that the knitted fiber maintains structural integrity and flexibility during hand knitting. Inspired by the myelinated structure of nerve axons, we demonstrate that ANF sheath facilitates efficient signal transmission, enabling woven textiles incorporating these fibers to support long-distance signal transfer (1.5 m), as shown in the textile-based touch-sensing prototype and display applications. These environmentally stable, knittable coaxial fibers exhibit potential for integration into wearable sensors, textile-based circuits, and wearable human–machine interface devices.

1 | Introduction

Smart textiles represent a transformative advance in textile technology. Recent developments in materials, fabrication, and device engineering have enabled the demonstration of advanced fabrics with integrated functionalities for energy harvesting and storage, sensing, and health monitoring applications, to name a few [1–3]. Realizing the necessary performance in these applications requires an effective, scalable approach for producing conductive fibers that incorporate electroactive materials [4–6]. However, producing fibers that simultaneously display high mechanical strength, flexibility, and electrical conductivity remains a challenge and requires advances in materials and fiber processing. For effective electrical communication in smart textiles, such fibers should demonstrate reliable long-distance signal transmission [7–9].

Over the past decade, a variety of electroactive materials have been incorporated into functional fibers, including carbon-based materials like carbon nanotubes (CNTs) [10, 11], and reduced graphene oxide (rGO) [12, 13], metal nanoparticles and nanowires [14, 15], and conducting polymers like polyaniline [16, 17] and poly(3,4-ethylenedioxythiophene):polystyrene sulfonate (PEDOT:PSS) [18]. Among these, $Ti_3C_2T_x$ (where T_x denotes surface functional groups), a member of the MXene family, stands out. MXenes offer several key advantages over carbon nanotubes,

graphene, and other carbon-based nanomaterials due to their unique combination of metallic conductivity, hydrophilicity, and programmable surface chemistry. Their intrinsic surface terminations (–O, –OH, and –F) provide strong interfacial bonding and tunable electrochemical behavior, enabling superior integration with polymers and active materials without sacrificing conductivity. Unlike the hydrophobic nature of CNTs and graphene, MXenes disperse readily in water, allowing uniform processing into films, fibers, and coatings [19, 20]. These synergistic properties make MXenes particularly advantageous for constructing high-performance, structurally controlled nanocomposites and next-generation wearable devices [21–24].

Significant progress has been made in producing MXene-based fibers, with coating and wet spinning emerging as practical and scalable strategies [25–29]. Coating involves depositing MXene onto substrate fibers such as nylon, cotton, or linen [4], which provides mechanical support for knitting and weaving [27]. However, MXene coatings are prone to delamination or peeling under mechanical deformation. In contrast, wet spinning offers greater versatility in dope composition and processing, capitalizing on the solution processability of MXenes in both aqueous and select organic solvents [30–33]. This method allows $Ti_3C_2T_x$ nanosheets to be combined with spinnable polymers or nanomaterials, producing hybrid fibers with enhanced mechanical and electrical properties [32, 34–38]. Although composite fibers of MXene and polymers show promise, inadequate control over internal microstructure and interfacial connectivity often compromises mechanical and electrical performance. MXene oxidation presents another challenge, particularly in coated yarns where the material is exposed to air [27, 28]. In practical applications, exposed conductive material in hybrid fibers can lead to short circuits when knitted or woven, disrupting conductive pathways, causing resistance fluctuations, and introducing significant signal noise [25, 27].

Recently, coaxial wet-spinning has gained increasing attention in the literature for producing high-performance MXene fibers (Table S1). Coaxial spinning provides a pathway to balance mechanical performance and functionality through independent control of core and sheath components. Nevertheless, coaxial wet spinning of MXene fibers remains in early development and requires further optimization. For example, Zhou et al. [39], produced ultracompact MXene fibers with an in situ-generated polycarbonate protective layer by leveraging interfacial interactions and thermal drawing-induced stresses. Li et al. [40] developed an MXene@ graphene oxide (GO) fiber with 50 wt.% GO loading as a supporting shell, achieving a tensile strength of 290 MPa and an electrical conductivity of 24 S cm^{-1}. Similarly, Liu et al. employed coaxial wet spinning to fabricate GO/MXene@cellulose [41] and MXene@ANF core–shell fibers [42] for applications in Joule heating and electromagnetic interference shielding. However, most spinning/coagulation methods rely on auxiliary chemical agents (e.g., polyelectrolytes, aldehyde crosslinkers, high-salt baths, surfactants, or organic cosolvents) to achieve spinnability and fiber solidification [21, 43–45]. These additives increase consumable and process-control costs, raise environmental and health burdens (VOC, toxicity, and wastewater treatment), and can degrade MXene performance by accelerating oxidation, inducing restacking, or leaving residues that reduce conductivity and hinder ion transport. Additionally, the use of different solvent systems for the MXene core and the polymeric sheath often creates incompatibility during co-coagulation, leading to phase separation, uneven solidification, and poor interfacial quality [44]. These additives also introduce interfacial instability (humidity-/pH-sensitive electrostatic complexes), modulus mismatch, and slippage under bending, while complicating continuous scale-up. Developing an additive-free aqueous coagulation approach holds great potential for enabling straightforward and scalable fabrication, reducing production costs, improving sustainability, and ensuring cleaner interfaces that enhance both mechanical reliability and electrochemical performance.

In this study, we fabricate MXene@ANF coaxial fibers using a coaxial wet-spinning technique and systematically investigate the coagulation process during fiber formation. We examine the influence of MXene dispersion concentration on morphological evolution and identify a bidirectional coagulation mechanism. The resulting coaxial fibers exhibit improved tensile strength and toughness compared to pristine MXene fibers, alongside high environmental stability and low electrical resistance. These properties make the fibers durable and suitable for knitting and weaving into textiles, as demonstrated in single-line signal transmission for capacitive touch sensors. Furthermore, the MXene@ANF fibers enable low-noise, reliable signal transmission in a textile-based touch sensing and display system. We anticipate that advances in coaxial fiber technology will support progress in smart textile applications, wearable technologies, and other applications requiring real-time data transmission. This is particularly relevant because as data demands increase, minimizing signal degradation and interference becomes increasingly critical for high-speed, accurate communication.

2 | Results and Discussion

Knittable, environmentally stable MXene@ANF fibers were fabricated using a coaxial wet-spinning process, as illustrated in Figure 1a. MXene and aramid nanofiber (ANF) dispersions were independently injected via two syringe pumps with a core-to-sheath volumetric ratio of 1:3 to ensure consistent linear spinning rates. This coaxial arrangement produced a stable core–sheath jet at the needle tip, which solidified into a well-defined fiber upon entering the coagulation bath. The resulting MXene@ANF fibers were collected on a spool after drying.

$Ti_3C_2T_x$ MXene was synthesized using a modified the minimally intensive layer delamination (MILD) method, as described in previous studies [46, 47]. X-ray diffraction (XRD) patterns confirmed complete etching of the Al layer, as indicated by the disappearance of the (104) and (105) peaks associated with the Al layer in Ti_3AlC_2 precursor material (Figure S1a). After washing and self-delamination, Ti_3AlC_2 particles (Figure S1b) were exfoliated into MXene nanosheets. Scanning electron microscopy (SEM) revealed nanosheets with lateral sizes of 3–5 μm (Figure 1b). Atomic force microscopy (AFM) confirmed a typical thickness of 1.5–1.7 nm for single-layer flakes (Figure 1c). The clean, sharp edges of the nanosheets indicate no significant oxidation, which helps preserve electrical conductivity [48, 49].

Kevlar-49 yarn was cut into 5 mm segments after washing with acetone and water. A solvent molecule intercalation method was used to improve exfoliation efficiency [50]. Finely ground potassium hydroxide (KOH) was mixed with dimethyl sulfoxide (DMSO)

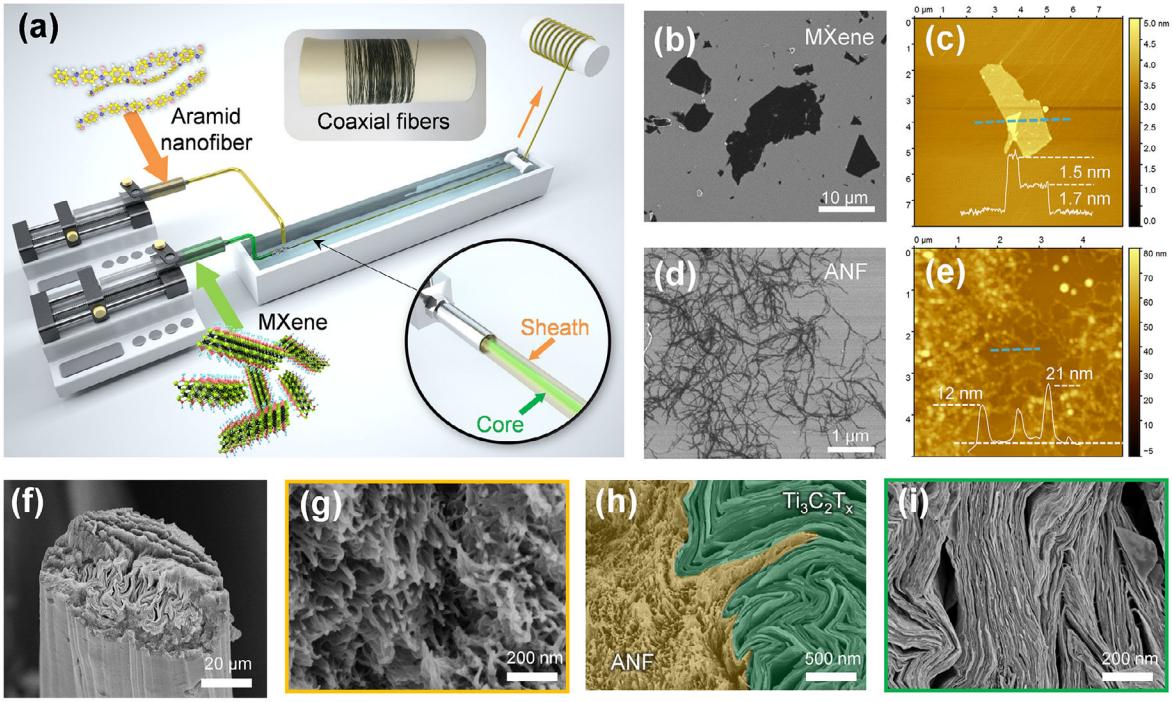

FIGURE 1 | (a) Schematic illustration of the coaxial wet-spinning setup used to fabricate MXene@ANF coaxial fibers. (b) SEM image and (c) AFM image of the single-layer MXene sheets on silicon wafer. (d) SEM image and (e) AFM image of ANF dispersion dried on silicon wafer. (f) SEM image of the cross-section of coaxial fiber prepared using a 35.4 mg mL^{-1} MXene dispersion. The magnified SEM image of the (g) well-aligned ANF sheath, (h) the interface between the ANF sheath and MXene core, and (i) closely packed MXene core.

and isopropanol (IPA), followed by theaddition of Kevlar yarn. The exfoliation of Kevlar yarn turned the mixture orange and increased its viscosity. The Kevlar yarn broke down into short fibers (Figure S1c), and after 2 h of stirring at 70°C, a homogeneous ANF dispersion formed (Figure S1d). SEM showed ANFs with high aspect ratios and lengths exceeding 5 μm (Figure 1d), while AFM indicated diameters of 10–20 nm (Figure 1e). The 1 wt.% ANF dispersion exhibited good spinnability, spontaneously forming microfibers when injected into a water bath. The resulting pure ANF fiber was light yellow and semi-transparent under optical microscopy, with a diameter of 25–30 μm (Figure S2a). Under crossed polarizers, the fiber showed clear birefringence (Figure S2b), indicating alignment along the fiber axis. The cross-section revealed a circular morphology with closely packed nanofibers (Figure S2c), confirming a dense internal structure.

In MXene@ANF coaxial fibers, polarized optical microscopy showed distinct optical birefringence in the ANF sheath surrounding the dark MXene core (Figure S3), confirming a well-defined core–sheath structure with uniform phase separation. The birefringence pattern resembled that of pure ANF fibers, suggesting aligned nanofibers in the sheath. Cross-sectional SEM images further verified a clear boundary between the ANF sheath and MXene core (Figure 1f–i). The ANF sheath contained highly aligned nanofibers, while the MXene core showed dense packing with nanosheets oriented along the fiber axis. This organized structure supports mechanical integrity and electrical conduction.

The measured area ratio of the MXene core to ANF sheath was approximately 1.6:3, slightly higher than the 1:3 cross-sectional area ratio of the spinning needle. This difference is attributed to the lower concentration of the ANF dispersion (1 wt.%) compared to the MXene dispersion (35.4 mg mL^{-1}), leading to a thinner sheath after drying. Coaxial fibers were also spun using a lower MXene concentration (10 mg mL^{-1}) to study the effect of dispersion concentration on morphology, as detailed in the following section.

Thermogravimetric analysis (TGA) in air showed a slight mass increase in pure MXene fibers above 500°C due to oxidation. Pure ANF fibers decomposed between 500°C and 550°C, with 4.6% mass remaining (Figure S4). This difference allowed estimation of the MXene/ANF mass ratio in coaxial fibers with 35.4 mg mL^{-1} of MXene; the core constituted ~64.1% of the fiber mass, decreasing to 31.7% at 10 mg mL^{-1}. The fibers maintained structural continuity even at lower concentrations, indicating that the coagulation process is less sensitive to dope concentration or viscosity than observed in graphene oxide-based systems [51].

To evaluate the mechanical properties of coaxial fibers, we compared stress–strain curves of MXene fiber [46], ANF fiber, ANF/MXene fiber [38], MXene/GO fiber [34], and MXene/PEDOT:PSS fiber [36]. The pure MXene fiber showed a tensile strength of ~40 MPa. The MXene/rGO composite fiber reached ~41 MPa with 50 wt.% MXene loading [34], while the PEDOT:PSS-based composite achieved ~75 MPa and a breaking strain of ~2.6% at the same MXene loading [36]. In contrast, the ANF/MXene composite fiber exhibited lower strength (~20 MPa at 50 wt.% of MXene loading) [38], likely due to the use of methanesulfonic acid and trifluoroacetic acid during ANF synthesis, which may have compromised dispersion quality [38].

Using the KOH and IPA method, we produced ANF fibers with a tensile strength of 336 MPa (Figure 2a). The high strength of the pure ANF fiber contributed significantly to the mechanical performance of the MXene@ANF coaxial fiber, owing to the densely

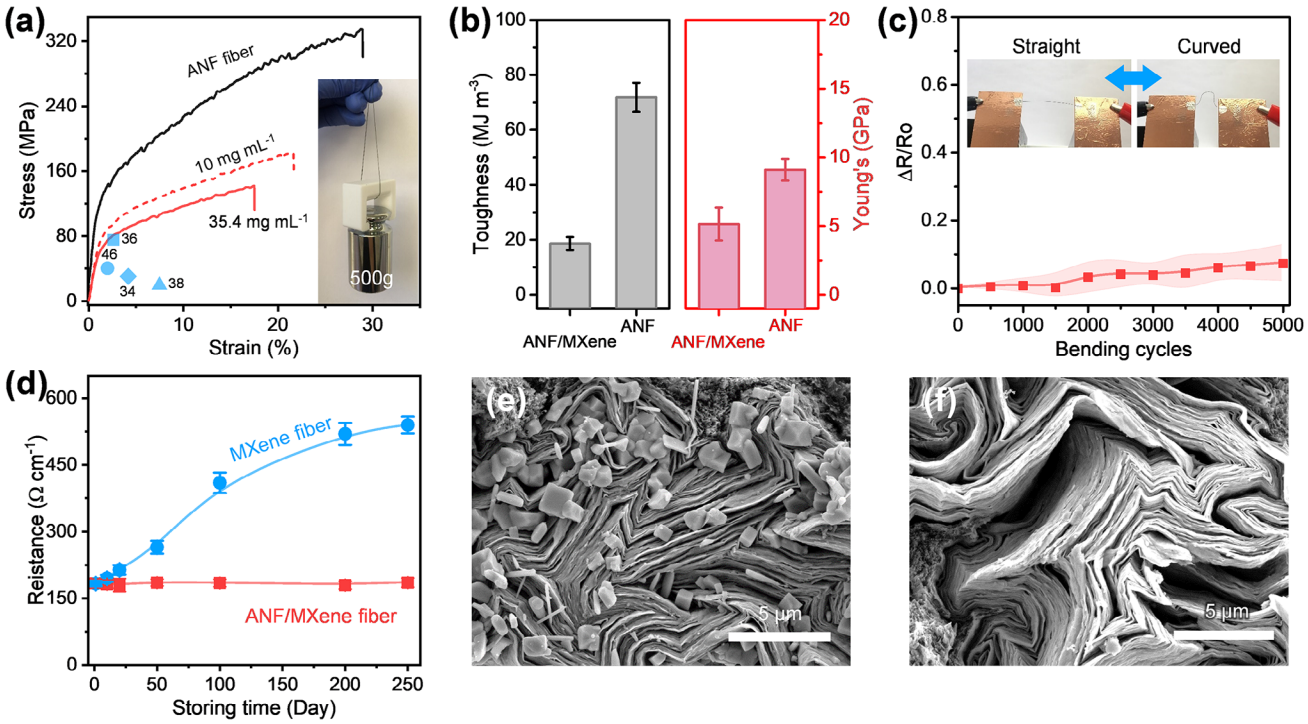

FIGURE 2 | (a) Stress–strain curves of MXene@ANF fibers prepared using 10 and 35.4 mg mL^{-1} MXene dispersions, compared to pure ANF fiber and literature values. (b) Toughness and Young's modulus of MXene@ANF fibers and pure ANF fiber. (c) Resistance changes in a 3-cm-long fiber over 5000 bending cycles, demonstrating mechanical–electrical durability. (d) Comparison of resistance of MXene and MXene@ANF fibers within 250 days of air exposure. SEM image of the MXene@ANF fiber (e) terminal and (f) a freshly fractured cross-section from the fiber midpoint after 250 days of air exposure, showing minimal structural degradation and oxidation in (f).

packed nanofibers in the sheath. The coaxial fiber spun with a 10 mg mL^{-1} MXene dispersion exhibited a breaking stress of 182.1 ± 5.6 MPa, higher than the 142.3 ± 4.1 MPa observed for fibers from a 35.4 mg mL^{-1} dispersion. The mechanical robustness was further demonstrated by the fiber's ability to lift a 500 g weight without failure. These results indicate that the continuous ANF sheath plays a critical role in the mechanical integrity of the coaxial fiber.

However, the inclusion of the MXene core reduced both toughness and Young's modulus (Figure 2b). The tightly stacked MXene nanosheets in the core provided consistent electrical connectivity. The MXene@ANF fiber showed a linear resistance of 185.3 ± 2.1 Ω cm^{-1} across increasing lengths (Figure S5), indicating uniform conductivity. The ANF sheath also helped maintain stable electrical resistance during repeated bending (Figures 2c and S6a), demonstrating strong mechanical–electrical durability.

We then monitored and compared the electrical resistance of MXene@ANF and pure MXene fibers over time to evaluate their environmental stability. We found that the resistance of MXene@ANF fiber remained stable for over 250 days (Figure 2d). In contrast, the pure MXene fiber showed a resistance increase from 179 to over 540 Ω cm^{-1} under the same conditions. These results indicate that the ANF sheath effectively protected the MXene core from atmospheric moisture. Additionally, the water-resistance test was performed by immersing the MXene@ANF fiber in water at room temperature for 20 min, followed by drying in a 60°C oven for 10 min to complete one cycle. After 20 such cycles, the MXene@ANF fiber maintained excellent mechanical and electrical stability, as shown in Figure S6b. Upon SEM analysis, cross-sectional images revealed that oxidation occurred mainly at the fiber ends, where the MXene core was exposed to air (Figure 2e), while the central region retained a well-defined MXene structure without visible TiO_2 particles (Figure 2f). This preservation of structure confirmed minimal oxidation and accounts for the sustained electrical performance of the MXene@ANF fiber. This difference highlights the importance of a protective sheath for long-term durability supporting its suitability as a durable conductive material for wearable and textile electronics.

To assess the mechanical flexibility of coaxial fibers, we hand knitted it into both flat and twisted ribbon configurations (Figures 3a and S7). Throughout the knitting process, which involved repeated twisting and bending at small length scales, SEM confirmed that the ANF sheath remained intact, without visible cracking or delamination. However, since SEM cannot evaluate the internal structure of the MXene core, we employed X-ray micro-computed tomography (micro-CT) [52] to leverage the high X-ray absorption contrast between MXene and ANF. A single CT slice clearly showed the boundary between the ANF sheath and MXene core, confirming the structural integrity of the coaxial architecture (Figure 3c). Due to its relatively low density, the ANF sheath was less distinct in the CT images compared to the MXene core, appearing as a transparent layer uniformly wrapped on the MXene core (Figure 3d). Cross-sectional SEM images further indicated that the MXene core retained its flat morphology after knitting. A frame from the 3D rotational micro-CT video (Video S1) also verified that the MXene core remained continuous despite mechanical deformation.

To evaluate the orientation and packing of MXene nanosheets within the fiber, we used wide-angle X-ray scattering (WAXS) analysis, in which the fiber axis was oriented parallel to the

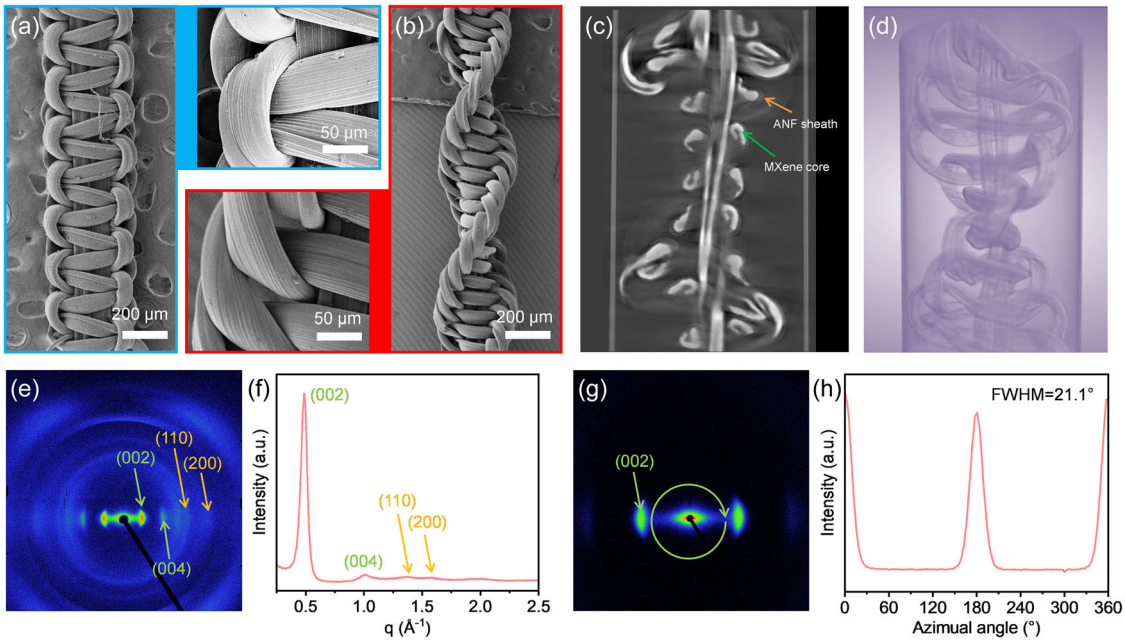

FIGURE 3 | SEM images of knitted MXene@ANF fiber in (a) flat and (b) twisted ribbon configurations. Insets show magnified views of the smooth fiber surface at bending positions. (c) A single slice from X-ray micro-computed tomography (micro-CT) of the woven fiber, revealing its internal structure. (d) The corresponding 3D reconstruction from micro-CT data, showing the continuous MXene core within the fiber (see Video S1). (e) Wide-angle X-ray scattering (WAXS) pattern of a vertically aligned MXene@ANF fiber. (f) Integrated scattering intensity along the equatorial direction (sector angle ± 5°), indicating anisotropic alignment. (g) SAXS/WAXS pattern highlighting the (002) diffraction signal from the MXene core. (h) Azimuthal intensity profile of the (002) reflection, confirming the alignment of MXene nanosheets along the fiber axis.

beam. The WAXS pattern (Figure 3e) displayed combined scattering features from both MXene [46] and ANF [53–55]. The 2D scattering pattern showed clear (002) and (004) MXene signals at *d*-spacings of 1.2 and 0.6 nm, respectively (Figure 3f), consistent with reported values for MXene structures [56, 57]. Weaker (110) and (200) peaks associated with π–π stacking in aramid molecules were also detectable [50, 55, 58]. To quantify the orientation of MXene sheets, we analyzed the azimuthal intensity distribution of the (002) peak using Herman's orientation function (f), where values near 1 indicate strong alignment of the sheets along the fiber axis. The MXene core exhibited an f value of ∼0.75 (Figure 3g,h), indicating noticeable alignment of nanosheets parallel to the fiber direction. This ordered stacking reduces the contact resistance of nanosheets and supports the high electrical conductivity observed in the MXene core [59, 60].

In coaxial spinning, the sheath solution must fully encapsulate the core material, making the viscosity of the sheath dope a key parameter. Achieving high performance at low MXene concentrations is significant for several reasons. First, reducing the MXene content lowers material costs and mitigates the issues associated with MXene oxidation while still maintaining excellent conductivity. Second, low-loading formulations greatly improve processability by preventing viscosity-induced clogging or aggregation during fiber spinning, allowing more uniform structures to be produced. Third, decreasing MXene content helps preserve the mechanical integrity of the composite; high MXene loadings typically lead to brittleness and reduced flexibility, whereas low-loading systems maintain high tensile strength and bending durability. The selected sheath material must be independently spinnable to support the formation of a stable core–sheath structure. While earlier studies indicate that the core solution has less stringent spinnability requirements than the sheath, core breakup can still occur, as observed in graphene oxide systems when the viscosity of core dope is too low [51]. This means the core fluid must also possess sufficient viscosity to ensure continuous flow without breakup during spinning. Compared with commonly used polymeric sheaths (e.g., PU and PDMS), the ANF sheath offers distinct structural and mechanical benefits. ANF forms a highly entangled, hydrogen-bonded nanofibril network with exceptional stiffness and toughness, allowing it to provide strong confinement and stable interfacial contact with the MXene core during deformation. In contrast, soft polymers such as PU or PDMS possess low modulus and weaker interfacial adhesion, which can lead to slippage or deformation mismatch under mechanical stress. The mechanically robust ANF sheath therefore ensures efficient load transfer, minimizes delamination, and maintains the structural integrity and electrical continuity of the coaxial fiber during repeated bending.

In our system, the MXene core remained continuous across both high and low concentrations, indicating favorable rheological properties for fiber formation. The ANF dispersion (1 wt.%) has an apparent viscosity of ∼50 Pa S at shear rate of 1 s^{-1} [61], while MXene dispersions at 35.4 and 10 mg mL^{-1} show viscosities of 2.1 and 0.2 Pa·S, respectively, at the same shear rate. The higher viscosity of the sheath aids in maintaining the shape of the core within the coagulation bath. Nevertheless, the substantial viscosity difference between core and sheath suggests that viscosity alone may not be the primary factor in coaxial structure formation, and other influences must be considered, for example, the interfacial interactions between core and sheath.

To develop an understanding of fiber formation and coagulation process using the MXene@ANF system as a model, we propose

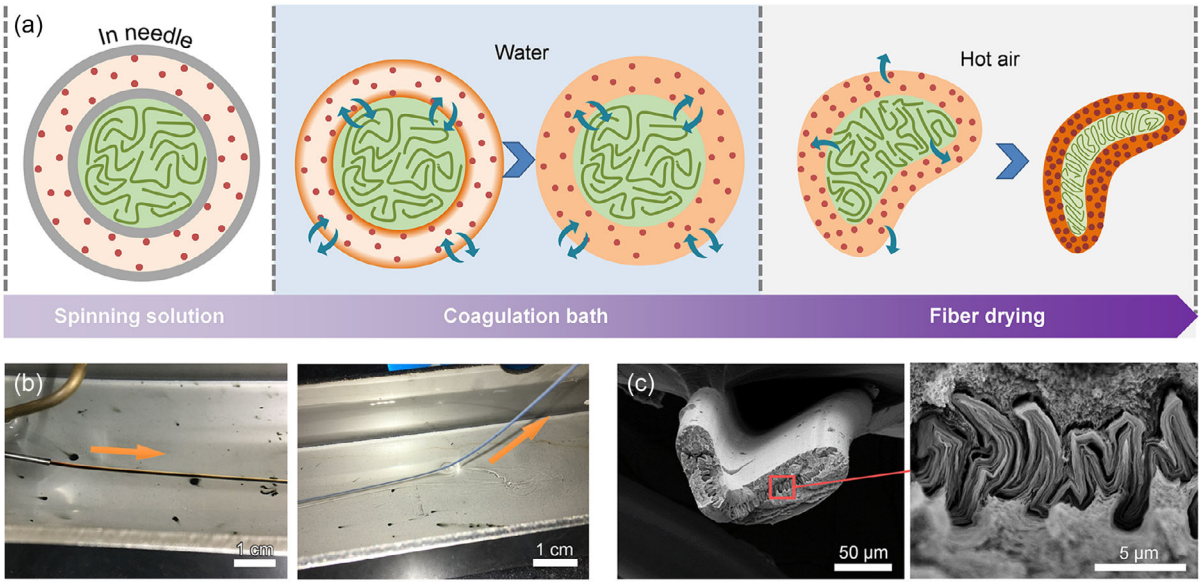

FIGURE 4 | (a) Schematic illustration of the bidirectional solidification mechanism during coagulation of the MXene@ANF fiber. (b) Photographs of the MXene@ANF fiber extruded in a water coagulation bath showing the initial transparent ANF sheath (left) and its transition to a white color (right) before being pulled out. (c) SEM image of the cross-section of a fiber produced using a low-concentration MXene dispersion (10 mg mL^{-1}).

that solvent compatibility and interfacial interactions play central roles in determining fiber morphology. As illustrated in Figure 4a, we suggest a bidirectional solidification mechanism during coagulation. Within the coaxial needle, the MXene dispersion and ANF solution remain separated by the needle wall, allowing each to align independently along the extrusion direction. After extrusion, the MXene dispersion contacts the ANF solution, while the ANF solution interfaces with the water bath. This setup enables simultaneous solvent exchange at two interfaces: (i) between the MXene core and ANF sheath and (ii) between the ANF sheath and the water bath. Bidirectional diffusion initiates coagulation from both inner and outer interfaces of ANF dispersion, promoting the development of a well-defined core–sheath structure.

The bidirectional solidification occurring at both the MXene–ANF interface and the ANF–water interface rapidly consolidates the ANF sheath. When ANF (initially dispersed in DMSO) is exposed to water, it undergoes rapid protonation, which disrupts the ANF–DMSO solvation structure and causes water to diffuse inward from the MXene core region toward the ANF sheath, forming a coherent core–sheath interface. Simultaneously, water from the coagulation bath diffuses into the ANF layer and replaces DMSO, leading to outward solidification and the formation of a robust outer sheath. The combination of these inward and outward solidification fronts ensures uniform sheath formation and strong interfacial adhesion.

As shown in Figure 4b, the ANF sheath initially forms a transparent brown layer surrounding the black MXene core at the needle outlet. With prolonged exposure to the water bath, the color of the ANF sheath changes to white and then light yellow before the fiber is fully dried and collected. Solidification occurs only in ANF sheath, while the MXene core maintains good dispersibility due to the excellent dispersibility of MXene in both water and DMSO. Final solidification of the MXene core occurs during drying, as the water/DMSO mixture diffuses and evaporates from the core outward. This process is accompanied by shrinkage of the ANF sheath, which applies compressive stress to the core, leading to a wrinkled and compacted MXene structure.

Fiber cross-sectional shape also depends on MXene concentration. As seen in Figures 1f and 4c, fibers with high-concentration MXene form a flat elliptical cross-section, while those with low-concentration MXene adopt a bent, ribbon-like morphology resembling certain natural fibers [4, 27]. During drying, significant volume shrinkage compresses the MXene core into a thin central layer, contributing to the ribbon-like form. The outer perimeter of the MXene core remains consistent (280 ± 40 μm) in both fiber types, supporting the proposed bidirectional coagulation mechanism. Solidification initiates at the inner MXene–ANF interface, defining the core boundary, and at the outer ANF–water interface, determining the fiber's external diameter.

A comparison with nerve fibers, whose myelin sheath insulates axons and facilitates rapid electrical conduction, reveals a conceptual similarity to the MXene@ANF fiber, where the ANF sheath acts as an insulating layer and the MXene core conducts electrical signals. To evaluate the coaxial fiber's suitability for signal transfer, we connected a piece of aluminum foil (as a touch pad) to a digital multimeter using the MXene@ANF fiber (Figure 5a). A computer-based data acquisition system recorded signal changes during testing. A 30-cm-long MXene@ANF fiber was woven into a fabric, with one half embedded in the textile and the other half exposed to air (Figure 5b).

To assess sensing performance, we measured the capacitance response when a dry finger touched different positions along the fiber (Video S2). As shown in Figure 5c, both the fiber and the aluminum touch plate exhibited a stable baseline capacitance of 15.7 ± 1.2 pF. No significant capacitance change occurred at Position #1 (on the woven section) and Position #2 (on the exposed fiber), indicating minimal interference or noise in the absence of direct touch. In contrast, capacitance increased markedly to 65.2 ± 2.3 pF when touching the aluminum foil (Position #3). This result confirms that both the woven and

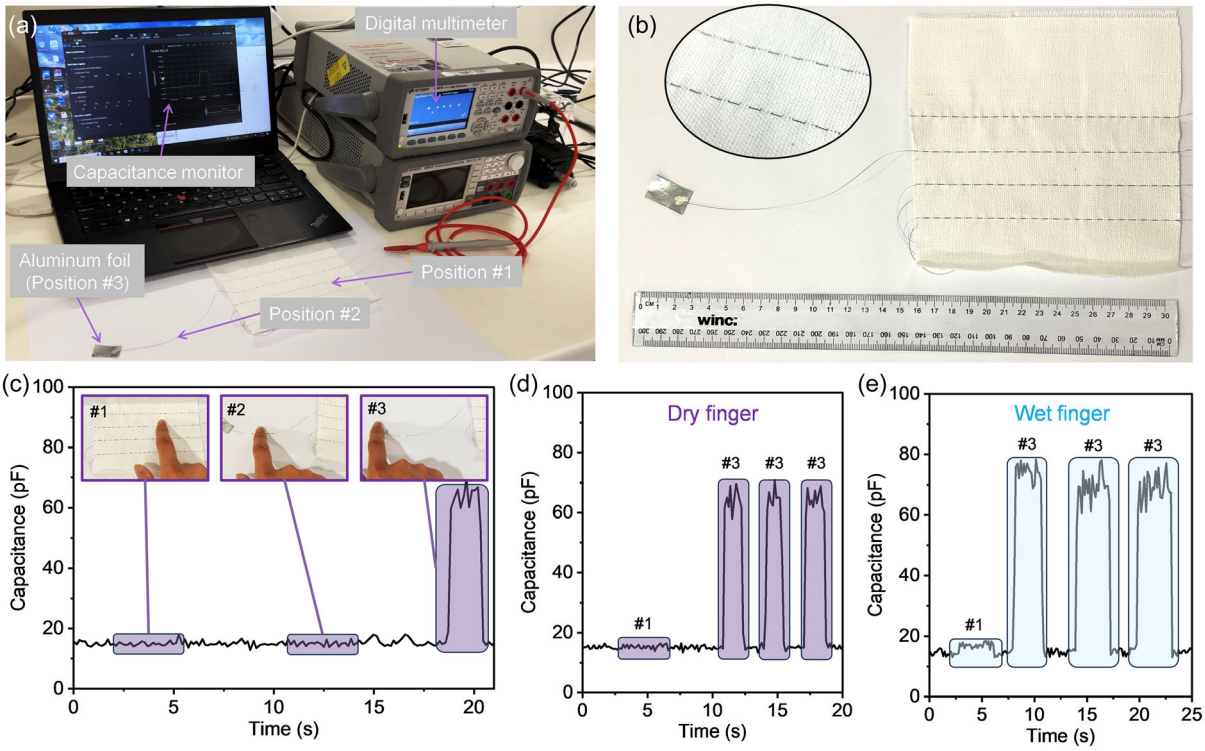

FIGURE 5 | (a) Photograph of the capacitive touch sensor setup using knitted MXene@ANF fiber integrated into a fabric. (b) Photograph of the knitted MXene@ANF fiber with a 1 cm × 2 cm aluminum foil attached to its terminal. (c) Capacitive response to a dry finger touching different positions (data extracted from Video S2). Signal response to (d) dry and (e) wet fingers at Position #1 and Position #3, respectively.

exposed segments of the coaxial fiber effectively protect signal integrity, with the aluminum foil serving as the primary signal source. The response also showed good repeatability (Figure 5d). When the copper wire was used as the connection cable, as shown in Figure S8, the touch pad generated a clear response upon finger contact. However, the copper wire also produced the same response when the finger touched the wire itself. This indicates that an unprotected metal conductor cannot function properly in a capacitive touch-sensor system, because the circuit interprets both the metal wire and the touch pad as part of the same effective sensing area. By contrast, when the MXene@ANF fiber served as the connection cable, only touches on the designated pad generated a signal, demonstrating that the sheath confines the electric field and suppresses parasitic coupling along the lead.

The analysis of the signal-to-noise ratio (SNR) shows that using the MXene@ANF fiber as the signal-transfer cable results in only a minimal change in SNR when the touch sensor is activated by either a dry or wet finger (Figure S9a). The SNR varies slightly from 11.7 to 16.4, demonstrating that the MXene@ANF

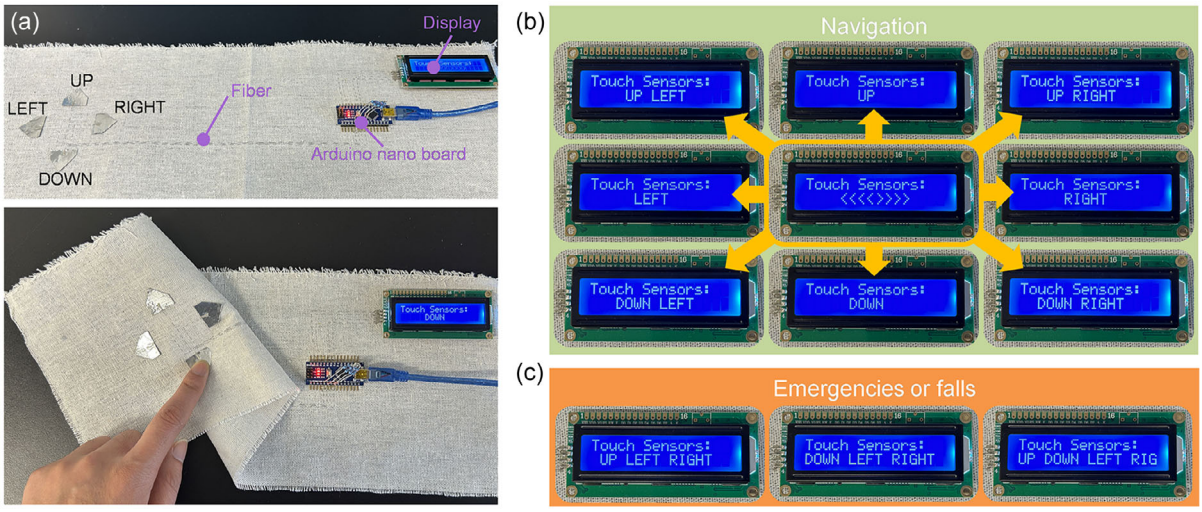

FIGURE 6 | (a) Touch sensor and control board integrated on textile, utilizing MXene@ANF fiber as the conductive wire; bottom image shows display response when the textile is folded. (b) Display response to single- and dual-direction touch inputs for navigation. (c) Display response to multiple simultaneous touches with clear identification for all direction, which can be identified as emergencies or falls.

fiber can maintain stable and reliable signal transmission under different contact conditions. Additionally, the MXene@ANF fiber exhibits a stable signal response without crosstalk when coaxial fibers are mechanically twisted together (Figure S9b).

We further examined the effect of fiber length on capacitive signal behavior by testing lengths from 1 to 150 cm (Figure S10). Both signal and background capacitance remained stable across all lengths. The coaxial fiber also maintained consistent signal shielding performance when contacted with wet fingers (Figure 5e). Touch at Position #3 with a wet finger resulted in a capacitance increase of ~10.5 pF (reaching 75.7 pF) due to the larger contact area from water absorption. In contrast, touch at Position #1 induced only a minor increase of ~4.1 pF demonstrating the effective signal protection provided by the ANF sheath. Therefore, the MXene@ANF fiber demonstrates outstanding signal protection capabilities under various conditions.

To validate its practical application, we integrated the fiber into a capacitive sensing and display system on a textile platform (Figure 6a) using an Arduino Nano as the control board. The system featured an LCD display that responded to directional touch inputs "LEFT," "RIGHT," "UP," and "DOWN" with a programmed response time of 50 ms. When no touch was detected, the display showed the default indicator "<<<<>>>>". As shown in Figure 6b and Video S3, the system was able to display eight directions using four touch pads. The system can also detect the combination of up to four touch pads (Figure 6c). This proof-of-concept system highlights potential applications in wearable safety devices, such as jackets that indicate a cyclist's turning direction or assistive navigation for visually impaired individuals. Remarkably, the embedded MXene@ANF fiber maintained signal integrity even under mechanical deformation of the textile, including bending, folding, and pressure (Videos S4 and S5). These results collectively demonstrate that MXene@ANF fibers enable robust, deformation-insensitive electronic textiles that are suitable for real-world wearable applications.

3 | Conclusion

In this study, we developed a coaxial spinning strategy that uses an ANF sheath to improve the alignment and stacking of MXene nanosheets within the core, producing MXene@ANF fibers with high mechanical strength, electrical conductivity, and environmental stability. Continuous core fibers were formed even at low MXene concentrations (10 mg mL^{-1}). A bidirectional solidification mechanism during coagulation explains the observed structural evolution, including the characteristic wrinkled cross-section of the fibers. Advanced X-ray characterization confirmed the fiber's structural integrity, supporting their integration into textiles and smart fabrics. Inspired by the biological role of the myelin sheath in nerve fibers, we demonstrated that the ANF layer not only enhances mechanical durability but also enables long-distance electrical signal transmission. This capability was illustrated through stable capacitive touch sensing, indicating the potential of these coaxial fibers for use in wearable sensors and signal-transmitting textiles.

4 | Experimental Section

4.1 | Preparation of ANF Dispersion

ANF dispersions were prepared from Kevlar thread using a solvent molecule intercalation method [50]. For a typical 1 wt.% ANF dispersion, 1.034 g of dried Kevlar 49 thread (DuPont UK) and 0.517 g of finely ground potassium hydroxide (KOH) were added to conical flask containing 90 mL dimethyl sulfoxide (DMSO). Under continuous stirring at 600 rpm, 10 g of isopropanol (IPA) was added. Stirring continues until complete disassembly of the microfiber was achieved (about 2 h), indicated by a dark red liquid with no residual fibers. The dispersion was centrifuged at 1200 rpm for 10 min to remove the undissolved KOH particles. The supernatant was collected and used directly as a spinning dope without further treatment.

4.2 | Synthesis of $Ti_3C_2T_x$ Dispersions

$Ti_3C_2T_x$ MXene was synthesized by etching Al atomic layers from Ti_3AlC_2 MAX phase (<40 μm particle size, Jilin 11 Technology Co., Ltd.), as previously described [46, 47]. The etching solution was prepared by dissolving 1.6 g lithium fluoride (LiF, 99%, Sigma–Aldrich) in 20 mL of 9 M hydrochloric acid (HCl, Sigma–Aldrich) with 5 min of stirring at room temperature. One gram of Ti_3AlC_2 powder was gradually added to the etchant, and the mixture was stirred at 35°C for 24 h. The acidic dispersion was washed with Milli-Q water via repeated centrifugation (Eppendorf 5810R) at 3500 rpm for 5 min per cycle until self-delamination occurred (pH ~ 6). The dispersion was vortex-mixed (Corning LSE) for 10 min and centrifuged at 1500 rpm for 10 min to isolate delaminated flakes. The supernatant containing single-layer MXene flakes was collected and further centrifuged at 8000 rpm for 10 min to obtain a spinnable MXene dispersion (35.4 mg mL^{-1}). A lower concentration dispersion (10 mg mL^{-1}) was prepared by diluting the concentrated MXene with Milli-Q water.

4.3 | Coaxial Spinning of MXene@ANF Fiber

Coaxial spinning was performed using two syringe pumps (KDS 100 Legacy Single Syringe Infusion Pump) and a custom needle assembly with 25G (core) and 19G (sheath) needles. MXene and ANF dispersions were loaded into separate 5 mL BD Tuberculin syringes. Extrusion rates were calculated based on needle cross-sectional areas to maintain a core-to-sheath volumetric ratio of 1:3 (e.g., core: 2.5 mL h^{-1} and sheath: 7.5 mL h^{-1}) and prevent relative movement during spinning (detailed parameters in Table S2). The extruded fiber entered a 1-m-long water coagulation bath for solvent exchange and solidification. Fibers were air-dried for 1 h on a scaffold before being would onto a spool.

4.4 | Characterization

Fiber and flake morphology was characterized using SEM (Hitachi S-4800) operating at an accelerating voltage of 5 kV. XRD patterns were acquired with a Rigaku Smart Lab powder diffractometer using Cu Kα radiation (0.03° step size and 0.5 s dwelling time). TGA was performed on a TA SDT Q600 instrument in air from room temperature to 800°C at 5°C min^{-1}. Flake and nanofiber thickness profiles were measured by atomic force

microscope using Nanosurf Flex AFM system with C3000i controller in a tapping mode with Tap300-G BudgetSensors probes. The AFM images were processed using Gwyddion V2.45. Tensile tests were conducted on a Shimadzu EZ-SX-50N with a 50 N loading cell (grip distance: 1 cm and strain rate: 1 mm min^{-1}). Young's modulus (E) was calculated using the tensile stress (σ) and strain (ε) from the linear elastic region:

$$E = \frac{\sigma}{\varepsilon} \tag{1}$$

Toughness (U_T) was determined by integrating the stress–strain curve:

$$U_T = \int_0^{\varepsilon_f} \sigma d\varepsilon \tag{2}$$

where ε_f is the failure strain.

Bending tests used a custom linear roller guide. Electrical resistance was measured with a Keysight 34460A multimeter using two needle electrodes. For insulated fibers, terminals were exposed by cutting and connected with silver paint. Capacitance was measured using a Keysight 34460A multimeter with the fiber connected to a 2 × 2 cm aluminum plate electrode. Small- and wide-angle X-ray scattering (SAXS/WAXS) data were collected on a Xeuss 3.0 beamline (Excillum MetalJet source, 9.2 keV, 250 W, wavelength of 1.3414 Å). Samples were measured at 100 mm detector distance (DECTRIS EIGER X 1 M detector, 75 µm pixel size, 10 min exposure). Data was processed using Xenocs XSACT Pro software. Herman's orientation factor (f) was calculated as

$$f = \frac{3<\cos^2\phi> - 1}{2} = \frac{\int_0^{2\pi} I(\phi)\cos^2\phi d\phi}{\int_0^{2\pi} I(\phi) d\phi} \tag{3}$$

where ϕ is the angle between the fiber axis and nanosheet alignment direction.

Author Contributions

Jizhen Zhang: conceptualization (lead), data curation (lead), investigation (lead), writing – original draft (lead), writing – review and editing (lead). **Sitarama Kada:** data curation (supporting), methodology (supporting), software (supporting), visualization (supporting). **Jian Tang:** methodology (supporting), software (supporting), visualization (supporting). **Jinlong Tao:** data curation (supporting), investigation (supporting), methodology (supporting), visualization (supporting), writing – original draft (supporting). **Peter A. Lynch:** data curation (supporting), methodology (supporting), supervision (equal), writing – original draft (supporting), writing – review and editing (supporting). **Renzhi Ma:** resources (supporting), supervision (supporting), visualization (supporting), writing – review and editing (supporting). **Joselito M. Razal:** conceptualization (supporting), investigation (supporting), methodology (supporting), supervision (lead), writing – original draft (supporting), writing – review and editing (supporting).

Acknowledgments

This work was supported by the National Natural Science Foundation of China (52203344), the Australian Research Council (IH210100023), and the Australian National Fabrication Facility (Victorian node at Deakin University). Additional support was provided by the Science and Technology Program of Hainan Province (ZDYF2020230 and ZDYF2022GXJS226). J.Z. acknowledges funding from the Alfred Deakin Postdoctoral Research Fellowship (FY2024) and the JSPS International Research Fellowship (24KF0273). J.M.R. acknowledges support from the Hong Kong Polytechnic University under the Strategic Hiring Scheme.

Funding

This work was supported by the National Natural Science Foundation of China (52203344), Australian Research Council (IH210100023), the Science and Technology Program of Hainan Province (ZDYF2020230 and ZDYF2022GXJS226), and Japan Society for the Promotion of Science (24KF0273).

Conflicts of Interest

The authors declare no conflicts of interest.

Data Availability Statement

The data that support the findings of this study are available from the corresponding author upon reasonable request.

References

1. J. Shi, S. Liu, L. Zhang, et al., "Smart Textile-Integrated Microelectronic Systems for Wearable Applications," *Advanced Materials* 32, no. 5 (2020): 1901958, https://doi.org/10.1002/adma.201901958.

2. J. Tabor, K. Chatterjee, and K. T. Ghosh, "Smart Textile-Based Personal Thermal Comfort Systems: Current Status and Potential Solutions," *Advanced Materials Technologies* 5, no. 5 (2020): 1901155, https://doi.org/10.1002/admt.201901155.

3. Y. Bai, Y. Zhou, X. Wu, et al., "Flexible Strain Sensors with Ultra-High Sensitivity and Wide Range Enabled by Crack-Modulated Electrical Pathways," *Nano-Micro Letters* 17, no. 1 (2024): 64, https://doi.org/10.1007/s40820-024-01571-6.

4. S. Uzun, S. Seyedin, A. L. Stoltzfus, et al., "Knittable and Washable Multifunctional MXene-Coated Cellulose Yarns," *Advanced Functional Materials* 29, no. 45 (2019): 1905015, https://doi.org/10.1002/adfm.201905015.

5. K. Dong, Y.-C. Wang, J. Deng, et al., "A Highly Stretchable and Washable All-Yarn-Based Self-Charging Knitting Power Textile Composed of Fiber Triboelectric Nanogenerators and Supercapacitors," *ACS Nano* 11, no. 9 (2017): 9490–9499, https://doi.org/10.1021/acsnano.7b05317.

6. S. Seyedin, S. Moradi, C. Singh, and J. M. Razal, "Continuous Production of Stretchable Conductive Multifilaments in Kilometer Scale Enables Facile Knitting of Wearable Strain Sensing Textiles," *Applied Materials Today* 11 (2018): 255–263, https://doi.org/10.1016/j.apmt.2018.02.012.

7. K. Zhang, X. Shi, H. Jiang, et al., "Design and Fabrication of Wearable Electronic Textiles Using Twisted Fiber-Based Threads," *Nature Protocols* 19, no. 5 (2024): 1557–1589, https://doi.org/10.1038/s41596-024-00956-6.

8. S. Hwang, M. Kang, A. Lee, et al., "Integration of Multiple Electronic Components on a Microfibre towards an Emerging Electronic Textile Platform," *Nature Communications* 13, no. 1 (2022): 3173, https://doi.org/10.1038/s41467-022-30894-4.

9. X. Wei, R. Li, S. Xiang, et al., "Smart Fiber with Overprinted Patterns to Function as Chip-Like Multi-Threshold Logic Switch Circuit," *Nature Communications* 16, no. 1 (2025): 7314, https://doi.org/10.1038/s41467-025-62648-3.

10. N. Behabtu, C. C. Young, D. E. Tsentalovich, et al., "Strong, Light, Multifunctional Fibers of Carbon Nanotubes with Ultrahigh Conductivity," *Science* 339, no. 6116 (2013): 182–186, https://doi.org/10.1126/science.1228061.

11. M. D. Lima, S. Fang, X. Lepró, et al., "Biscrolling Nanotube Sheets and Functional Guests into Yarns," *Science* 331, no. 6013 (2011): 51–55, https://doi.org/10.1126/science.1195912.

12. S. Seyedin, J. M. Razal, P. C. Innis, R. Jalili, and G. G. Wallace, "Compositional Effects of Large Graphene Oxide Sheets on the Spinnability and Properties of Polyurethane Composite Fibers," *Advanced Materials Interfaces* 3, no. 5 (2016): 1500672, https://doi.org/10.1002/admi.201500672.

13. J. Zhang, S. Seyedin, Z. Gu, et al., "Liquid Crystals of Graphene Oxide: A Route Towards Solution-Based Processing and Applications," *Particle & Particle Systems Characterization* 34 (2017): 1600396, https://doi.org/10.1002/ppsc.201600396.

14. M. Zhao, D. Li, J. Huang, D. Wang, A. Mensah, and Q. Wei, "A Multifunctional and Highly Stretchable Electronic Device Based on Silver Nanowire/Wrap Yarn Composite for a Wearable Strain Sensor and Heater," *Journal of Materials Chemistry C* 7, no. 43 (2019): 13468–13476, https://doi.org/10.1039/C9TC04252K.

15. T. Gao, Z. Yang, C. Chen, et al., "Three-Dimensional Printed Thermal Regulation Textiles," *ACS Nano* 11, no. 11 (2017): 11513–11520, https://doi.org/10.1021/acsnano.7b06295.

16. J.-G. Kim, D.-M. Lee, J. Y. Jung, et al., "Hybrid Polyaniline/Liquid Crystalline CNT Fiber Composite for Ultimate Flexible Supercapacitors," *ACS Applied Energy Materials* 4, no. 2 (2021): 1130–1142, https://doi.org/10.1021/acsaem.0c02217.

17. F. Zhang, P. A. Halverson, B. Lunt, and M. R. Linford, "Wet Spinning of Pre-Doped Polyaniline into an Aqueous Solution of a Polyelectrolyte," *Synthetic Metals* 156, no. 14 (2006): 932–937, https://doi.org/10.1016/j.synthmet.2006.06.002.

18. J. Zhang, S. Seyedin, S. Qin, et al., "Fast and Scalable Wet-Spinning of Highly Conductive PEDOT:PSS Fibers Enables Versatile Applications," *Journal of Materials Chemistry A* 7, no. 11 (2019): 6401–6410, https://doi.org/10.1039/C9TA00022D.

19. Y. Zhou, Y. Zhang, Y. Pang, et al., "Thermally Conductive Ti3C2Tx Fibers with Superior Electrical Conductivity," *Nano-Micro Letters* 17, no. 1 (2025): 235, https://doi.org/10.1007/s40820-025-01752-x.

20. P. Zhou, G. Jiang, Y. Wang, Y. Tian, and X. Zhang, "Self-Adaptive and Large-Area Sprayable Thermal Management Coatings for Energy Saving," *Nature Communications* 16, no. 1 (2025): 3791, https://doi.org/10.1038/s41467-025-59259-3.

21. F. Yang, X. Zhao, K. A. S. Usman, et al., "Engineering Coaxial MXene@CNT Fibers via Wet-Spinning for Balanced Mechanical, Electrical, and Electrochemical Performance," *Journal of Energy Storage* 137 (2025): 118719, https://doi.org/10.1016/j.est.2025.118719.

22. K. A. S. Usman, J. Zhang, L. Bi, et al., "The Future of MXene Fibers," *Advanced Materials* 37, no. 36 (2025): 2506437, https://doi.org/10.1002/adma.202506437.

23. X. Chu, Y. Wang, L. Cai, et al., "Boosting the Energy Density of Aqueous MXene-based Supercapacitor by Integrating 3D Conducting Polymer Hydrogel Cathode," *SusMat* 2, no. 3 (2022): 379–390, https://doi.org/10.1002/sus2.61.

24. B. Zhou, M. Yuan, H. Lu, et al., "Large-Area Knittable, Wash-Durable, and Healable Smart Fibers for Dual-Modal Sensing Applications," *Advanced Functional Materials* 34, no. 40 (2024): 2404064, https://doi.org/10.1002/adfm.202404064.

25. L. Bi, W. Perry, R. Wang, et al., "MXene Functionalized Kevlar Yarn via Automated, Continuous Dip Coating," *Advanced Functional Materials* 34, no. 14 (2024): 2312434, https://doi.org/10.1002/adfm.202312434.

26. Q. Liang, K. Liu, T. Xu, et al., "Interfacial Modulation of $Ti_3C_2T_x$ MXene by Cellulose Nanofibrils to Construct Hybrid Fibers with High Volumetric Specific Capacitance," *Small* 20, no. 17 (2024): 2307344, https://doi.org/10.1002/smll.202307344.

27. A. Levitt, D. Hegh, P. Phillips, et al., "3D Knitted Energy Storage Textiles Using MXene-Coated Yarns," *Materials Today* 34 (2020): 17–29, https://doi.org/10.1016/j.mattod.2020.02.005.

28. A. Levitt, J. Zhang, G. Dion, Y. Gogotsi, and J. M. Razal, "MXene-Based Fibers, Yarns, and Fabrics for Wearable Energy Storage Devices," *Advanced Functional Materials* 30, no. 47 (2020): 2000739, https://doi.org/10.1002/adfm.202000739.

29. Y. Zhou, Y. Zhang, K. Ruan, et al., "MXene-Based Fibers: Preparation, Applications, and Prospects," *Science Bulletin* 69, no. 17 (2024): 2776–2792, https://doi.org/10.1016/j.scib.2024.07.009.

30. S. Abdolhosseinzadeh, X. Jiang, H. Zhang, J. Qiu, and C. Zhang, "Perspectives on Solution Processing of Two-Dimensional MXenes," *Materials Today* 48 (2021): 214–240, https://doi.org/10.1016/j.mattod.2021.02.010.

31. B. Akuzum, K. Maleski, B. Anasori, et al., "Rheological Characteristics of 2D Titanium Carbide (MXene) Dispersions: A Guide for Processing MXenes," *ACS Nano* 12, no. 3 (2018): 2685–2694, https://doi.org/10.1021/acsnano.7b08889.

32. S. Seyedin, S. Uzun, A. Levitt, et al., "MXene Composite and Coaxial Fibers with High Stretchability and Conductivity for Wearable Strain Sensing Textiles," *Advanced Functional Materials* 30, no. 12 (2020): 191054, https://doi.org/10.1002/adfm.201910504.

33. Q. Zhang, H. Lai, R. Fan, P. Ji, X. Fu, and H. Li, "High Concentration of $Ti_3C_2T_x$ MXene in Organic Solvent," *ACS Nano* 15, no. 3 (2021): 5249–5262, https://doi.org/10.1021/acsnano.0c10671.

34. S. Seyedin, E. Yanza, and J. M. Razal, "Knittable Energy Storing Fiber with High Volumetric Performance Made from Predominantly MXene Nanosheets," *Journal of Materials Chemistry A* 5, no. 46 (2017): 24076–24082, https://doi.org/10.1039/C7TA08355F.

35. A. Levitt, S. Seyedin, J. Zhang, et al., "Bath Electrospinning of Continuous and Scalable Multifunctional MXene-Infiltrated Nanoyarns," *Small* 16, no. 26 (2020): e2002158, https://doi.org/10.1002/smll.202002158.

36. J. Zhang, S. Seyedin, S. Qin, et al., "Highly Conductive $Ti_3C_2T_x$ MXene Hybrid Fibers for Flexible and Elastic Fiber-Shaped Supercapacitors," *Small* 15, no. 8 (2019): e1804732, https://doi.org/10.1002/smll.201804732.

37. X. Zhu, Y. Zhang, Z. Man, et al., "Microfluidic-Assembled Covalent Organic Frameworks@$Ti_3C_2T_x$ MXene Vertical Fibers for High-Performance Electrochemical Supercapacitors," *Advanced Materials* 35, no. 46 (2023): 2307186, https://doi.org/10.1002/adma.202307186.

38. B. Cheng and P. Wu, "Scalable Fabrication of Kevlar/$Ti_3C_2T_x$ MXene Intelligent Wearable Fabrics with Multiple Sensory Capabilities," *ACS Nano* 15, no. 5 (2021): 8676–8685, https://doi.org/10.1021/acsnano.1c00749.

39. T. Zhou, Y. Yu, B. He, et al., "Ultra-Compact MXene Fibers by Continuous and Controllable Synergy of Interfacial Interactions and Thermal Drawing-Induced Stresses," *Nature Communications* 13, no. 1 (2022): 4564, https://doi.org/10.1038/s41467-022-32361-6.

40. X. Chen, J. Jiang, G. Yang, C. Li, and Y. Li, "Bioinspired Wood-Like Coaxial Fibers Based on MXene@graphene Oxide with Superior Mechanical and Electrical Properties," *Nanoscale* 12, no. 41 (2020): 21325–21333, https://doi.org/10.1039/D0NR04928J.

41. L.-X. Liu, W. Chen, H.-B. Zhang, et al., "Tough and Electrically Conductive Ti3C2T MXene–based Core–shell Fibers for High–performance Electromagnetic Interference Shielding and Heating Application," *Chemical Engineering Journal* 430 (2022): 133074, https://doi.org/10.1016/j.cej.2021.133074.

42. L.-X. Liu, W. Chen, H.-B. Zhang, et al., "Super-Tough and Environmentally Stable Aramid. Nanofiber@MXene Coaxial Fibers with Outstanding Electromagnetic Interference Shielding Efficiency," *Nano-Micro Letters* 14, no. 1 (2022): 111, https://doi.org/10.1007/s40820-022-00853-1.

43. L. Ye, L.-X. Liu, M. Jin, et al., "Interfacial Confinement Derived High-Strength MXene@Graphene Oxide Core-Shell Fibers for Electromagnetic Wave Regulation, Thermochromic Alerts, and Visible Camouflage," *Small* 21, no. 11 (2025): 2411735, https://doi.org/10.1002/smll.202411735.

44. L. Ye, L.-X. Liu, G. Yin, et al., "Highly Conductive, Hydrophobic, and Acid/Alkali-Resistant MXene@PVDF Hollow Core-Shell Fibers for Efficient Electromagnetic Interference Shielding and Joule Heating," *Materials Today Physics* 35 (2023): 101100, https://doi.org/10.1016/j.mtphys.2023.101100.

45. G. Zhao, C. Sui, L. Miao, et al., "Strong and Continuous MXene/Sodium Alginate Composite Fibers Prepared by Immersion Rotary Jet Spinning Process with Outstanding Electromagnetic Interference Shielding Performance," *Chemical Engineering Journal* 469 (2023): 143983, https://doi.org/10.1016/j.cej.2023.143983 doi:.

46. J. Zhang, S. Uzun, S. Seyedin, et al., "Additive-Free MXene Liquid Crystals and Fibers," *ACS Central Science* 6, no. 2 (2020): 254–265, https://doi.org/10.1021/acscentsci.9b01217.

47. K. A. S. Usman, J. Zhang, D. Y. Hegh, et al., "Sequentially Bridged $Ti_3C_2T_x$ MXene Sheets for High Performance Applications," *Advanced Materials Interfaces* 8, no. 7 (2021): 2002043, https://doi.org/10.1002/admi.202002043.

48. J. Zhang, N. Kong, D. Hegh, et al., "Freezing Titanium Carbide Aqueous Dispersions for Ultra-Long-Term Storage," *ACS Applied Materials & Interfaces* 12, no. 30 (2020): 34032–34040, https://doi.org/10.1021/acsami.0c06728.

49. J. Zhang, D. Hegh, P. A. Lynch, and J. M. Razal, "Guidelines on MXene Handling and Storage Strategies," in *Transition Metal Carbides and Nitrides (MXenes) Handbook*, (John Wiley & Sons, Inc, 2024), 163–188.

50. Z. M. Han, Y. Hou, H. C. Liu, et al., "Fast and Massive Production of Aramid Nanofibers via Molecule Intercalation," *Journal of the American Chemical Society* 147, no. 9 (2025): 7939–7949, https://doi.org/10.1021/jacs.4c18620.

51. A. Mirabedini, J. Foroughi, B. Thompson, and G. G. Wallace, "Fabrication of Coaxial Wet-Spun Graphene–Chitosan Biofibers," *Advanced Engineering Materials* 18, no. 2 (2016): 284–293, https://doi.org/10.1002/adem.201500201.

52. B. Soltan Mohammadlou, S. Ippolito, J. FitzPatrick, P. Upadhyay, T. L. Burnett, and Y. Gogotsi, "Characterization of MXene-Based Materials by X-Ray Computed Tomography," *Small Methods* 9, no. 8 (2025): 2500262, https://doi.org/10.1002/smtd.202500262.

53. D. Lee, J. Cho, J. G. Son, and B. Yeom, "Highly Aligned Aramid Nanofibrillar Nanocomposites for Enhanced Dynamic Mechanical Properties," *Composites Part B: Engineering* 229 (2022): 109467, https://doi.org/10.1016/j.compositesb.2021.109467.

54. T. Christoff-Tempesta, Y. Cho, D.-Y. Kim, et al., "Self-Assembly of Aramid Amphiphiles into Ultra-Stable Nanoribbons and Aligned Nanoribbon Threads," *Nature Nanotechnology* 16, no. 4 (2021): 447–454, https://doi.org/10.1038/s41565-020-00840-w.

55. H. Ji, S. Feng, and M. Yang, "Controlled Structural Relaxation of Aramid Nanofibers for Superstretchable Polymer Fibers with High Toughness and Heat Resistance," *ACS Nano* 18, no. 28 (2024): 18548–18559, https://doi.org/10.1021/acsnano.4c04388.

56. K. A. S. Usman, J. Zhang, C. J. O. Bacal, et al., "Tension-Induced Toughening and Conductivity Enhancement in Sequentially Bridged MXene Fibers," *2D Materials* 9, no. 4 (2022): 044003, https://doi.org/10.1088/2053-1583/ac8c51.

57. J. Zhang, N. Kong, S. Uzun, et al., "Scalable Manufacturing of Free-Standing, Strong $Ti_3C_2T_x$ MXene Films with Outstanding Conductivity," *Advanced Materials* 32, no. 23 (2020): 2001093, https://doi.org/10.1002/adma.202001093.

58. L. Si, R. Song, H. Xiao, et al., "A Mechanically Robust, Extreme Environment-Stable, and Fast Ion Transport Nanofluidic Fiber," *Nano Letters* 25, no. 11 (2025): 4494–4502, https://doi.org/10.1021/acs.nanolett.5c00097.

59. K. A. S. Usman, J. Zhang, K. P. Marquez, et al., "Recent Advances and Opportunities in MXene -based Liquid Crystals," *InfoMat* 6, no. 3 (2024): e12516, https://doi.org/10.1002/inf2.12516.

60. J. Zhang, K. A. S. Usman, M. A. N. Judicpa, D. Hegh, P. A. Lynch, and J. M. Razal, "Applications of X-Ray-Based Characterization in MXene Research," *Small Methods* 7, no. 8 (2023): e2201527, https://doi.org/10.1002/smtd.202201527.

61. M. Li, X. Chen, X. Li, J. Dong, X. Zhao, and Q. Zhang, "Controllable Strong and Ultralight Aramid Nanofiber-Based Aerogel Fibers for Thermal Insulation Applications," *Advanced Fiber Materials* 4, no. 5 (2022): 1267–1277, https://doi.org/10.1007/s42765-022-00175-2.

Supporting Information

Additional supporting information can be found online in the Supporting Information section. **Supporting Fig. S1:** (a) XRD patters of $Ti_3C_2T_x$ MXene and its Ti_3AlC_2 MAX phase precursor. (b) SEM image of Ti_3AlC_2 particles. Photographs showing the dissolving process of Kevlar yarn after (c) 30 min and (d) 2 h. **Supporting Fig. S2:** Optical images of ANF fiber under polarized microscope (POM) with (a) parallel and (b) perpendicular alignment of the analyzer and polarizer. (c) SEM image of the ANF fiber cross-section. (d) Magnified view of nanofibers exposed at fracture sites. **Supporting Fig. S3:** Polarized optical microscopy (POM) images of an ANF fiber under (a) parallel and (b) cross-polarized light. **Supporting Fig. S4:** Thermogravimetric analysis (TGA) of pure MXene, pure ANF fiber, and MXene@ANF fibers spun from different MXene dispersion concentrations. **Supporting Fig. S5:** Electrical resistance of the MXene@ANF fiber as a function of length. Resistance was measured using a two-electrode configuration with direct connection to a multimeter. **Supporting Fig. S6:** (a) SEM image of the MXene@ANF fiber after 100 bending cycles. (b) Changes of mechanical strength and electrical resistance of MXene@ANF fiber during the water-resistance test. **Supporting Fig. S7:** Schematic illustration of hand knitting of the half-square knot and square knot of MXene@ANF fibers. **Supporting Fig. S8:** The touch sensor response when a copper wire was used as the connection cable. **Supporting Fig. S9:** (a) The signal-to-noise ratio changes when the touch sensor is touched by dry and wet fingers. (b) Signal response between adjacent fibers. **Supporting Fig. S10:** Capacitance of the background and signal as a function of MXene@ANF fiber length. **Supporting Table S1:** Summarized progress and applications of MXene coaxial fibers in literature. **Supporting Table S2:** Spinning parameters during coaxial spinning. **Supporting Video S1:** Three-dimensional imaging of MXene@ANF coaxial fibers. **Supporting Video S2:** Capacitance change measurement using KEYSIGHT 34465A digital multimeter. **Supporting Video S3:** MXene@ANF fibers embedded in flat textile with Arduino Nano board. **Supporting Video S4:** MXene@ANF fibers embedded in folded textile with Arduino Nano board. **Supporting Video S5:** MXene@ANF fibers embedded in textile with Arduino Nano board—under pressure.